nature

SUPPLEMENTARY INFORMATION

https://doi.org/10.1038/s41586-019-1114-6

In the format provided by the authors and unedited.

Nanosecond X-ray diffraction of shock-compressed superionic water ice

Marius Millot[1,3]*, Federica Coppari[1,3]*, J. Ryan Rygg[1,2], Antonio Correa Barrios[1], Sebastien Hamel[1], Damian C. Swift[1] & Jon H. Eggert[1]

[1]Lawrence Livermore National Laboratory, Livermore, CA, USA. [2]Laboratory for Laser Energetics and Department of Mechanical Engineering, University of Rochester, Rochester, NY, USA. [3]These authors contributed equally: Marius Millot, Federica Coppari. *e-mail: millot1@llnl.gov; coppari1@llnl.gov

CONTENTS

S1. TARGETS AND LASER-DRIVEN SHOCK COMPRESSION

Double-distilled, deionized water is encapsulated in a 1.5 mm diameter cavity within a $30\mu m$ thick polyimide film, sealed by two diamond plates without any metallic or anti-reflection coatings. The diamonds are 2 mm diameter, single crystal with <110> orientation and about 20-30 μm (ablator) or 50-100 μm (window) thick. The $C/H_2O/C$ package is glued and centered on a $150\mu m$ thick Ta foil having a $500\mu m$ diameter pinhole, and placed on the PXRDIP diagnostic box. White-light interferometry measurements are used to determine the water layer thickness.

The water targets are shock compressed by direct-drive laser ablation at the Omega Laser Facility, Laboratory for Laser Energetics (LLE) of the University of Rochester, NY (USA) using 100-200 J of 351 nm UV light delivered by 6 laser beams having a 23° angle incidence and focused with 1.8-m-focal-length, f/6 optics. A composite pulse shape of about 15 ns of total length is obtained by firing the six beams (having a 1 or a 3.7 ns-long pulse shape) in sequence. SG8 distributed phase plates are used to smooth the laser imprint and to create a $\sim$ 900 μm diameter, flat-top super-gaussian spatial distribution at the focal spot. The focal spot being much larger than the thickness of the target package ensures a one-dimensional compression during the duration of the experiments. Laser-driven shock compression is destructive: a new target is necessary for each experiment or laser *shot*.

S2. LINE-IMAGING ULTRAFAST DOPPLER VELOCIMETRY

We use the Velocity Interferometer System for Any Reflector (VISAR) to document the compression history for each experiment. At the Omega Laser Facility, two VISAR channels offer a line-imaging, time-resolved record of the velocity of moving reflecting interfaces and optical properties (reflectivity, absorptivity) at the probe laser wavelength, 532 nm. Fringe motion is recorded on streak cameras. The fringe phase encodes the velocity history while the fringe amplitude contains information about the reflectivity of the tracked moving interface and the absorptivity of the medium that the probe laser is passing through[38,39]. VISAR velocity per fringe (VPF) sensitivities are 1.644 km/s/fringe and 2.732 km/s/fringe for the two channels. Velocity uncertainties, estimated as $\sim 5\%$ of the VPF, are 0.08 and 0.14 km/s. 2 GHz timing fiducial combs are recorded for each image on both streak cameras, allowing us to accurately correct timing for sweep nonlinearities.

In the absence of any dielectric or metallic coatings, the $C/H_2O/C$ package is initially transparent and contains several weakly reflecting interfaces that are simultaneously tracked by the VISAR. The most intense signal comes from the 17% Fresnel reflection at the diamond window/vacuum interface, and allows us to monitor the free-surface velocity u_{FS} (see Figure 1, Supplementary Figure 1, Supplementary Figure 2 and Supplementary Figure 3). Before the compression waves exceed the diamond Hugoniot elastic limit, causing the window to lose its transparency, weaker reflections at the ablator-sample and sample-window interfaces contribute to beating signatures that indicate the beginning and end of the first shock transit accross the water layer (see Supplementary Figure 1). Excellent planarity is observed on the VISAR data over the $500\mu m$ diameter view through the x-ray collimating aperture.

S3. HYDRODYNAMIC SIMULATIONS

A. Settings and optimization

We carry out post-shot simulations of the laser-driven compression of each experiment. HYADES is a one-dimensional, Lagrangian, radiation-hydrodynamic code[40] which uses a leapfrog time integration and artificial viscosity. The $150\mu m$ thick target package is divided into $\sim$ 600 material zones.

We use tabular opacities from the Lawrence Livermore National Laboratory LEOS database, and equation of state (EOS) tables from both the LEOS and the Los Alamos National Laboratory Sesame databases. For the laser-plasma interaction at the ablation front, we use the Thomas-Fermi ionization model and a flux-limiter equal to 3% of the free stream value, which has been found to provide meaningful results at similar intensities[41] up to $\sim 1TW/cm^2$.

We strive to use the most accurate models available to date to simulate our experiments. Unfortunately, there is no multi-phase equation of state for water that describes correctly both the solid and superionic ices as well as the dense liquid. Of course this is a consequence of the extreme polymorphism of water: building such a model is a complex task. We use LEOS 2010 as well as Sesame 7154 in order to estimate the influence of a different EOS on the final result.

LEOS 2010 is found to capture quite well the compressibility of dense H_2O in the regime studied here. We show how this model and others compare with currently available data in the pressure-density space in Figure S4 of Ref. [16]. In addition, Figure S11 of Ref.[16] also shows that LEOS 2010 captures well the shock temperature along the principal Hugoniot of liquid water. We therefore expect this model to also accurately describe the temperature rise in the early stages of the multi-shock compression that we used in the present study. Finally, Supplementary Figure 15 shows that LEOS 2010 reproduces the prediction of the most advanced model from Ref.[15] regarding the isentropic compression of water ice relevant for the later stages of the multi-shock compression in the present study. In our benchmarking tests, Sesame 7154 predictions appears only slightly less accurate.

For diamond we use the EOS tables Sesame 7834 and LEOS 64[42]. We use a pressure hardening Steinberg-Guinan model parameterized according to density-functional-theory simulations to account for the yield strength of diamond[43]. The diamond shear modulus is $G(P) = G_0(1 + A\ P\ \eta^{-1/3})$ where we use $G_0 = 540\ GPa$ as the shear modulus in the (110) direction, $A = 4.3\ 10^{-3}\ GPa^{-1}$ and η is the compression ratio $\eta = \rho/\rho_0$.

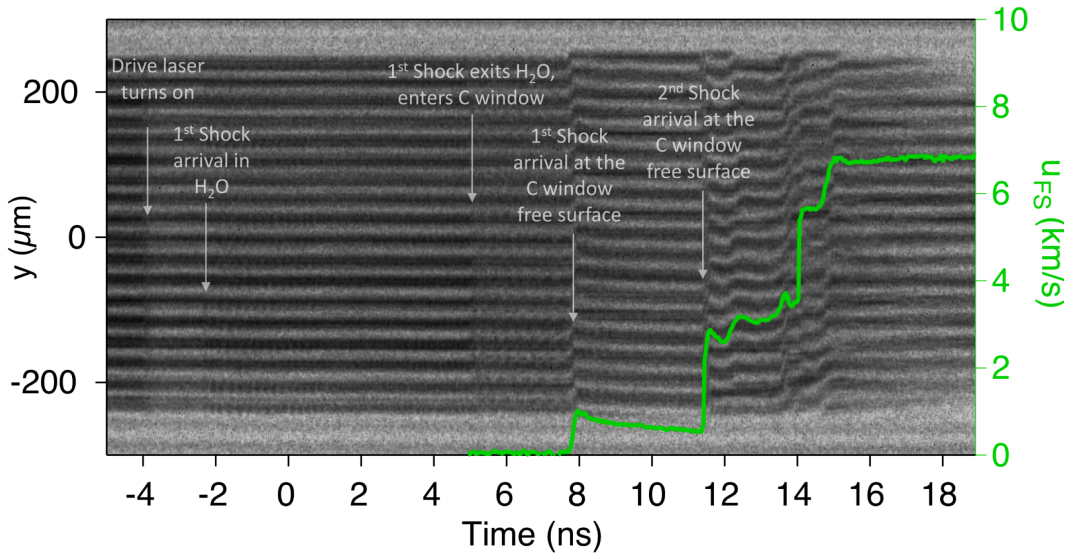

Supplementary Figure 1. **Representative VISAR data for shot 75758.** The $C/H_2O/C$ target package has no metallic or anti-reflection coatings, and is therefore transparent with small Fresnel reflections at the different interfaces, dominated by the 17% reflectivity of the diamond window free surface. A loss of reflectivity is observed when the drive laser turns on due to the beginning of the ablation process at the C ablator. Intensity *beatings* created by the extra reflection at the moving shock front indicate the arrival time and breakout time of the leading shock front in the water layer[44]. At later times, the VISAR fringe motion shows the arrival of the leading shock at the free surface, followed by the subsequent shocks leading to the progressive acceleration of the free surface.

The yield strength is $Y(P) = Y_0\ G(P)/G_0$ with $Y_0 = 70\ GPa$. The H_2O sample layer is considered to behave as a fluid. The longitudinal pressure P_L, continuous at the C/H_2O interfaces, is obtained as $P_L = P - \sigma_D$, σ_D being the deviatoric stress.

The measured drive-laser pulse-shape for each shot is used as an initial guess. Intensity multipliers are then applied in an iterative way to constrain the simulated free surface velocity u_{FS} to match the measured u_{FS} (Figure 1 and Supplementary Figure 3) and the arrival times of the leading shock at the ablator-sample and sample-window interfaces. Several simulations are conducted for each shot to evaluate the influence of different EOS models, as well as the use of slightly different intensity multipliers producing equally good agreement with the measured U_{FS}. We find that the final pressure and temperature conditions during the x-ray exposure calculated with LEOS 2010 or Sesame 7154 do not differ by more that a few %.

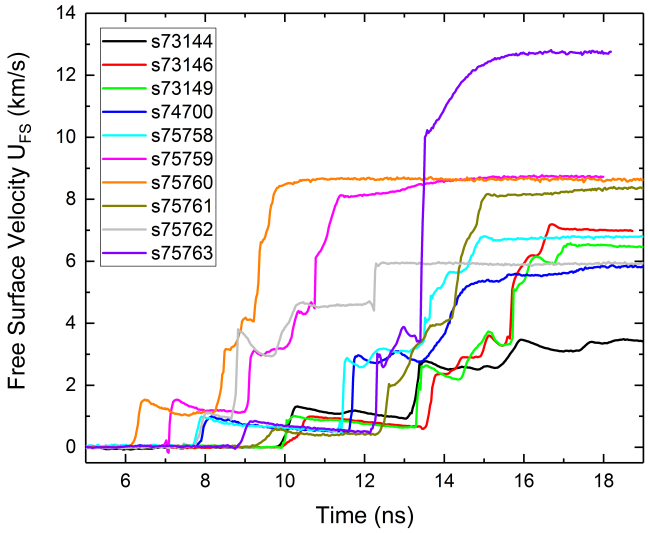

Supplementary Figure 2. **Free Surface velocity histories for all shots.** u_{FS} time histories obtained from the data collected with the most sensitive VISAR channel and spatially averaged over the 500 μm diameter of the x-ray collimating aperture.

B. Pressure-temperature determination

We interrogate each simulation to determine the pressure and temperature states of the H_2O during the pulsed-x-ray exposure. Specifically we compute pressure and temperature histograms for the computational zones containing H_2O during the duration of the 1 ns x-ray exposure to evaluate their statistical distribution. We calculate the average values P_i and T_i and the standard deviation $\sigma(P)_i$ and $\sigma(T)_i$ for each simulation. The final values of P and T, $\sigma(P)$ and $\sigma(T)$ are obtained by averaging the results of the different simulations *e.g.* $P = \overline{(P_i)}$ and $\sigma(P) = \overline{\sigma(P)_i}$. $\sigma(P)$ and $\sigma(T)$ therefore represent the inhomogeneity of the P-T conditions within the H_2O layer during the x-ray snapshot. For all shots, we find that the average of the standard deviation is larger than the standard deviation of the averages: $\sigma(P) > SD(P_i)$ and $\sigma(T) > SD(T_i)$.

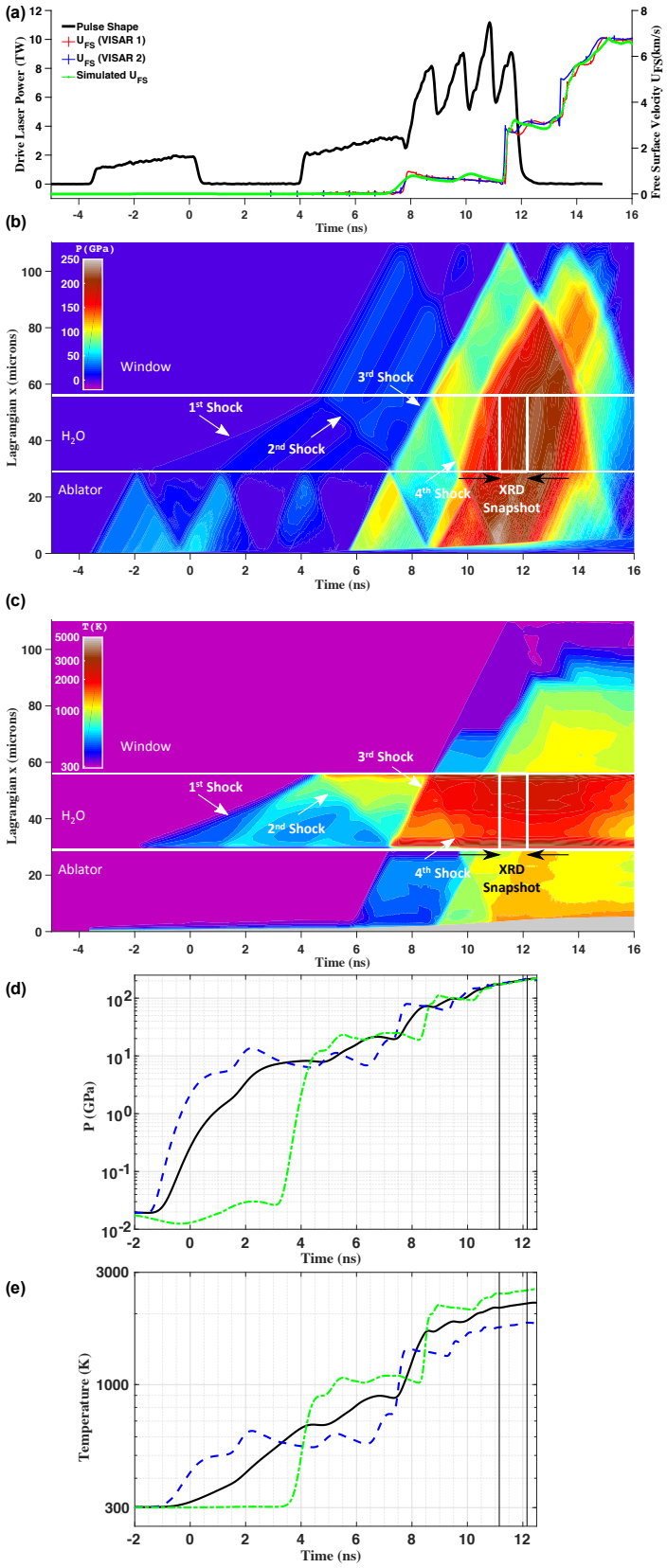

Supplementary Figure 3. **Determination of the reverberation compression path using one-dimensional Lagrangian hydrodynamic simulations constrained by velocimetry measurements. (a)** Measured drive-laser pulse shape for shot 75758 (black curve) and resulting experimental free-surface velocity U_{FS}(red and blue curves corresponding to the two VISAR channels), overlayed with simulated u_{FS} (green curve) matching both the arrival time and amplitude of the compression waves. **(b)** and **(c)** Corresponding longitudinal pressure and temperature space-time contour maps as obtained from hydrodynamic simulations. **(d)** and **(e)** Corresponding time histories for one zone near the ablator (dash blue), one zone near the window (dash-dot green) and averaged over the full water layer (solid black) illustrate the step-wise reverberation compression. Cross-timing between the drive-laser, the x-ray source laser and the VISAR diagnostic allow us to determine the time of the XRD snapshot (white rectangle/vertical black lines). Final determination of the pressure and temperature of the H_2O during the XRD snapshot is obtained by averaging the results of several simulations.

S4. X-RAY DIFFRACTION SETUP AND DATA ANALYSIS

We use up to 16 laser beams delivering 8 kJ of 351 nm UV light in a 1 ns super-gaussian flat-top pulse to irradiate – with a 300 μm spot size – a 12 μm thick Fe foil positioned $\sim$25 mm away from the water target at $\sim$45° angle. The laser intensity is tuned to generate primarily He-α radiation at 6.7 keV, with lower intensities satellite emissions at lower and higher energies (Supplementary Figure 4).

The Powder X-Ray Diffraction Image Plate (PXRDIP) diagnostic is a 50×50×75 mm box, containing image plate detectors used to record the diffraction patterns at the Omega Laser Facility. The diagnostic has an aperture in the front plate to hold the target and an additional aperture in the back plate to allow simultaneous VISAR measurements. A detailed description is available in Ref.[18].

Raw image plate data are geometrically projected into ϕ (azimuthal angle around the direction of the direct x-ray beam)-2θ (Bragg angle) space, to obtain straight lines of constant 2θ. The projection is done using the diffraction signal from the Ta aperture behind the target package as a reference.

Note that the Ta XRD lines originate from the outermost surface of the Ta pinhole collimating aperture. This is because the absorption depth of Ta at 6.7 keV for photons incident at $\sim$45° is 2μm, therefore only the x-rays that get diffracted at the back surface of the Ta can be transmitted, scattered and collected on the image plate detector without being absorbed. Because this surface is in vacuum and normal stress has to be conserved across an interface, the pressure of the Ta that contributes to the XRD is constrained to $\ll 1bar$ to match the surrounding medium.

One-dimensional integration of the XRD data is performed to obtain diffraction intensity as a function of Bragg angle (see Supplementary Figure 5 and Supplementary Figure 6 with lineouts in red). This is performed after masking out the bright spots due to the single crystal diamond (when close to the water ice peak), that are however shown in the projected image for completeness. White "patches" in the raw images visible in some of the shots are regions of the image plates masked out before doing the one-dimensional integration because they contain spurious signal (*e.g.* shadowing or fluorescence from different sources). These features are shown in some of the shots to highlight that there is no assignment ambiguity with diffraction signal.

The various diffraction peaks shown in Supplementary Figure 5 and Supplementary Figure 6 are assigned to either Ta at ambient conditions (reference material used to calibrate the diffraction geometry[18]), compressed diamond or compressed water ice. Because the x-ray source emission is not purely monochromatic (Supplementary Figure 4), reflections due to the satellite emission are also visible in the XRD patterns in addition to the diffraction due to the main x-ray energy (6.7 keV for the He-α radiation of the Fe x-ray source).

Using the 1D lineouts, each water diffraction peak is fit to a gaussian curve to obtain the 2θ angle from which the d-spacing and, assuming a structure, the density, can be calculated.

The uncertainty in the d-spacing is obtained from the propagation of the uncertainty in 2θ which we estimate by adding in quadrature three contributions: (i) the uncertainty in finding the centroid of the diffraction line with the gaussian fit, (ii) the displacement of the observed Ta reference lines from their ideal 2θ positions, that accounts for the quality of the geometrical projection, and (iii) the estimated angular broadening due to the distribution of compression states in the water sample during the x-ray snapshot. This contribution is estimated by assuming that water ice strength is weak enough so that the statistical distribution of compression states reflects the stress distribution in the sample. Using the equation of state models found to be in good agreement with our data in Figure 3, we infer a $\Delta\rho_{Inhom.}$ from the ΔP reported in Supplementary Table 2, from which we obtain an approximated contribution to the angular broadening $\Delta 2\theta_{Inhom}$.

The gaussian fits of the XRD intensity lineouts as a function of 2θ also provide a measure of the observed angular broadening through the determination of the full-width at half-maximum FWHM(2θ) for each H_2O peak (see Supplementary Table 2). This broadening has several contributions including geometrical effects due to the spatial extent of our x-ray source and collimation scheme[18], the finite spectral bandwidth of the x-ray source[18], compression inhomogeneity throughout the sample, and grain-size effects. Using the Scherrer equation and the total observed FWHM(2θ) therefore yields a lower bound for the typical grain size: $D = B\lambda/(\mathrm{FWHM}(2\theta) \times \cos(\theta))$ where λ is the x-ray wavelength, B a geometrical factor (we assumed $B = 0.9$) and θ is the Bragg angle[45].

We show all the diffraction data with a complete peak assignment in Supplementary Figure 5 and Supplementary Figure 6.

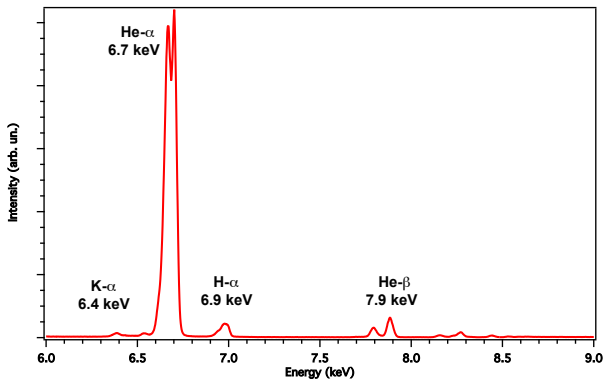

Supplementary Figure 4. **Iron x-ray source spectrum**. Typical experimental spectrum of the x-ray radiation generated by the irradiation of an iron foil with $\sim$5 TW of laser power in a 1 ns flat-top pulse focused on a 300 μm focal spot, as measured in shot 75758. The main line emission (He-α) is accompanied by satellite emissions at lower and higher energies.

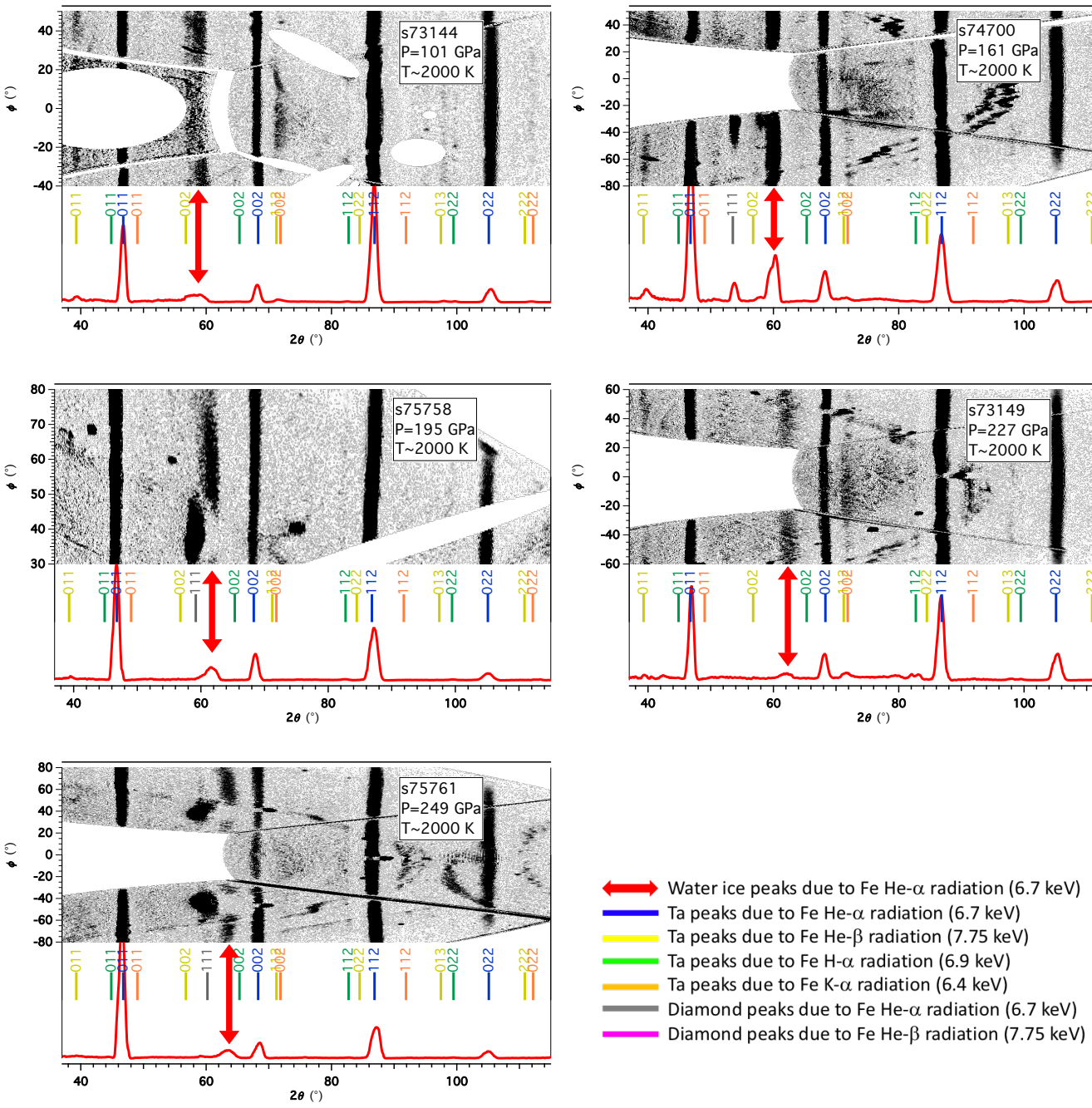

Supplementary Figure 5. **Diffraction data for the experiments probing the *bcc* structure.** Image-plate detector data projected in ϕ-2θ space. Red curves are XRD intensity lineouts. Peak assignment is shown by a vertical line and the Miller indices of the corresponding reflection.

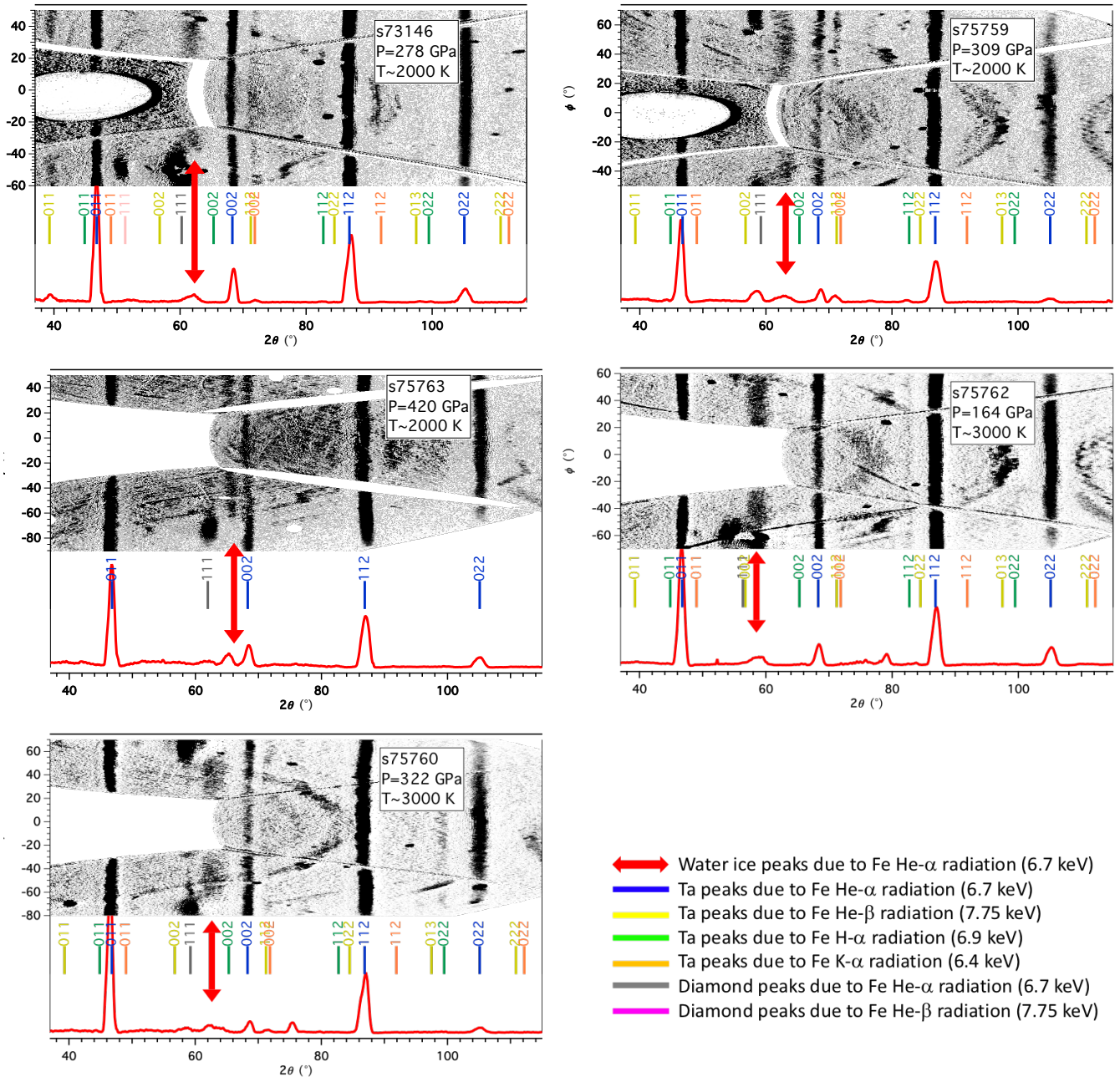

Supplementary Figure 6. **Diffraction data for the experiments probing the *fcc* structure.** Image-plate detector data projected in ϕ-2θ space. Red curves are XRD intensity lineouts. Peak assignment is shown by a vertical line and the Miller indices of the corresponding reflection.

S5. INTERPRETATION OF THE XRD RESULTS

A. Evidence for the *bcc* to *fcc* phase transition

Our data evidence a solid-solid phase transition occurring above 270 GPa along the quasi-isentrope near 2,000 K (Figure 3b). In all the diffraction data we only observe one diffraction peak from water ice. This does not allow us to perform a structural refinement, however we can test different structures and check for consistency in d-spacing and/or density. In particular, fitting the observed peak to a given structure should give a density value between the principal isentrope and the principal Hugoniot curves and should not generate large volume discontinuity across phase transitions (according to density functional theory simulations[15]).

The measured d-spacings for water ice as a function of pressure are reported in Figure 3b. Below 270 GPa our measurements (blue circles) agree with the position of the (110) reflection of a *bcc* lattice, as shown by the comparison with the position of the *bcc*(110) reflection calculated from DFT-derived equations of state[27] (blue dotted curve). For comparison in Figure 3b we show also the position of the (110) peak at room temperature inferred from the volume reported in Ref.[26] and obtained from diamond anvil cell static compression experiments (black dashed curve). As expected, because of thermal expansion, we measure a larger d-spacing than room temperature static compression experiments. If we now calculate the density for the *bcc*-like water ice and compare our data to the literature in pressure-density space, we obtain good agreement with the measured stress-density profile for water ices below ∼200 GPa (Figure 3c). For completeness additional DAC datasets from the literature are shown in density-pressure space (Refs.[26,33–37]). Consistently with the observation done for the d-spacing, our data are shifted to lower density relative to room temperature DAC data at the same pressure because of the higher temperature (∼2,000 K and ∼3,000 K) in our experiments.

Above 270 GPa we observe a discontinuity in d-spacing (red circles in Figure 3b), that is a signature for a solid-solid phase transition. Our interpretation is that the solid lattice of oxygens undergoes a *bcc*-to-*fcc* transformation. Indeed, if we assign the observed peak to the (111) reflection of a *fcc* lattice we obtain the density values reported in Figure 3c with red circles. The densities obtained at these pressures are reasonable and the absence of a large density jump at the transition further supports our assignment. The same *fcc* lattice is stable along the quasi-isentrope near 3,000 K (red squares).

B. Other potential interpretations that can be ruled out

1. *No phase transformation, all data correspond to a bcc structure*

Fitting the measured d-spacing to the (110) peak of a *bcc* lattice for all shots induces a 8% density drop at 270 GPa (Supplementary Figure 7), that is an extraordinary large expansion of the crystal. The temperature increase with increasing pressure along the quasi-isentrope near 2,000 K is quite small so that – according to both the experimental and theoretical EOS models – thermal expansion cannot be invoked to explain such density drop with increasing pressure along the ∼ quasi-isentrope near 2,000 K (comparing the blue and the red circles). In addition, comparison of the high temperature isotherms calculated from the DFT simulations[15] at 2,000K and 3,000 K (red dashed and red dot-dashed lines in Supplementary Figure 7) indicates that thermal expansion is unlikely to account for a 8% density drop between 2,000K and 3,000 K (comparing the blue circles and the red squares). We can therefore rule out this interpretation.

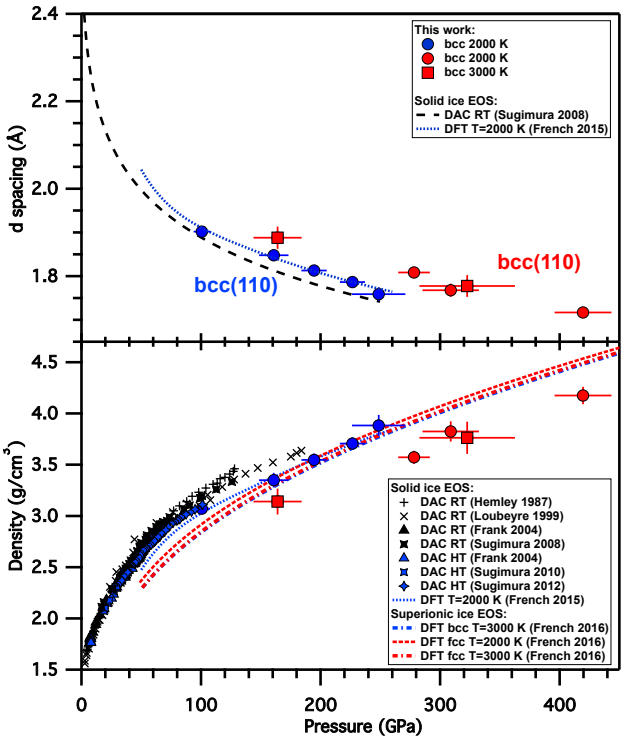

Supplementary Figure 7. **d-spacing and density vs pressure assuming a *bcc* lattice at all pressures (*i.e.* no phase transition)**. Fitting the d-spacings measured above 270 GPa to a *bcc* lattice produces an unphysical density drop, not explained by thermal expansion (see text).

2. *Transformation to a Pbcm structure*

Theoretical calculations at T=0K predict that water will transform to an orthorhombic structure with space group *Pbcm* above 400 GPa[28,29]. Considering the structural parameters and their evolution as a function of pressure reported in[28], we calculate the expected diffraction pattern for this structure at 400 GPa (see inset in Supplementary Figure 8). The XRD pattern for the *Pbcm* structure is characterized by five closely spaced peaks in the angular region around 2θ=65° where we observe the diffraction signal for water ice. The most intense peak is the (111) reflection and the other four peaks are more

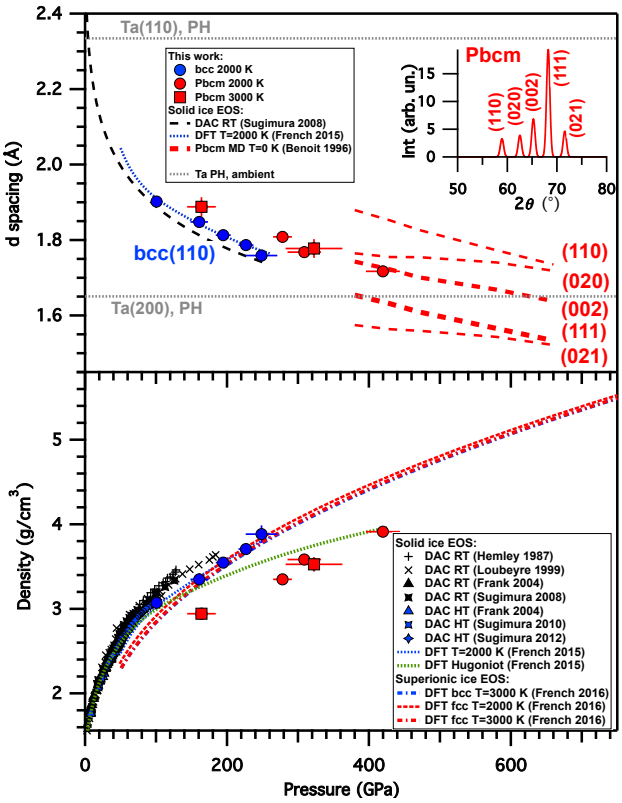

Supplementary Figure 8. **Comparison of the measured d-spacings and density vs pressure with the *Pbcm* structure**. Upper panel: Our data are represented by circles and squares for data collected along the quasi-isntropes near 2,000 K and 3,000 K respectively. Blue symbols are used for *bcc* ice and red for the new phase. The red dashed lines represent the expected d-spacings for the *Pbcm* structure as obtained in[28]. The thickness of the lines corresponds to the diffraction peak intensity. The horizontal gray dotted lines represent the d-spacings for of the ambient conditions Ta lines. The inset shows the calculated diffraction pattern (intensity versus Bragg angle) for the *Pbcm* structure at 400 GPa and 0 K as obtained in[28]. The calculation is done considering the wavelength used in the actual experiment (λ=1.85 Å) and the peak broadening accounts for the experimental angular resolution (2θ $\sim$0.8°). Lower panel: Red circles and squares represent the density of water ice assuming the *Pbcm* is the stable structure above the phase transition. The density is obtained by fitting the measured d-spacing to the (111) reflection. This leads to an unphysical density discontinuity of $\sim$13% across the phase transition with densities lower than the density of *bcc* solid ice along the Hugoniot of ice VII calculated using a DFT-MD equation of state[27](green dotted line).

than a factor of two less intense.

In the main plot of Supplementary Figure 8 (upper panel) we compare the measured d-spacing with the expected positions of the reflections for the *Pbcm* structure (red dashed lines, where the thickness of each line corresponds to the peak intensity). The expected position of the (111) peak (the most intense) does not correspond to the observed diffraction from water. The only peak for the *Pbcm* structure that could fit our data is the (002) reflection. However its intensity is more than a factor of two lower than the (111) reflection, therefore one would expect to see at least two lines and not just an isolated peak. Overlap with the Ta(200) reference peak (gray dotted line) could potentially explain the "missing" of the (111) reflection only for the highest pressure shot. It would not be a satisfactory explanation however, since at 420 GPa the two peaks are very close, but not perfectly overlapping, so that one would expect to see two closely spaced lines or at least peak broadening, and these signatures are not seen in the data (Supplementary Figure 6, shot 75763).

It is arguable that because the molecular dynamics simulations in[28] were performed at 0 K, thermal expansion could shift the (111) peak to higher d-spacings so to match the observed diffraction peak in our experiments. In this scenario the water ice would undergo a 13% density drop at 270 GPa (Supplementary Figure 8, lower panel). Such a big density discontinuity is in contrast with the expectation of small volume change for these transitions[15,27,31] and would result in a density even lower than the density of *bcc* solid ice along the Hugoniot of ice VII (green dotted line), which is unphysical. In addition, a compression-driven structural change is expected to result in a more compact structure, not a more open one, as the density drop associated with the *bcc-Pbcm* transition would imply.

We can therefore rule out this interpretation.

3. *Transformation to a hcp structure*

Formation of superionic ices with an *hcp* (hexagonal closed packed) lattice of oxygens has been predicted by theoretical simulations[14]. Assuming ideal c/a=1.63, the corresponding diffraction pattern would consist of three closely spaced peaks [(100), (002) and (101)], where the (101) reflection would be the most intense and the other two peaks would have similar intensities. Supplementary Figure 9 shows the density of the water ice if we were to assign the observed diffraction peak to the (101) reflection, *i.e.* the most intense peak. It is clear that this would generate a sudden large crystal expansion at the transition and would also bring the density below the density of *bcc* solid ice along the Hugoniot of ice VII (green dotted line).

If we assume that the observed peak is due to the *hcp* (100) reflection, then the calculated density would be higher than the cold curve for *bcc* water ice, which again is unphysical, considering the final temperatures obtained upon ramp compression are around 2,000-3,000 K (Supplementary Figure 10).

The only assignment that would give an acceptable density is assuming the observed peak is the *hcp* (002) (Supplementary Figure 11). However, as can be observed in Supplementary Figure 12, in this case we should have observed also the (101) peak that is the most intense peak for the *hcp* structure. The relative position of the *hcp* triplet peaks will change by varying the c/a. However the only way the *hcp* structure can satisfactorily fit our data is to have the (002) at 65° to match the observed peak of water ice and the (101) at 68.5° to explain its absence by the overlap with the Ta(200) line. There is no c/a value for an *hcp* lattice that can generate such a pattern.

We can therefore rule out this interpretation.

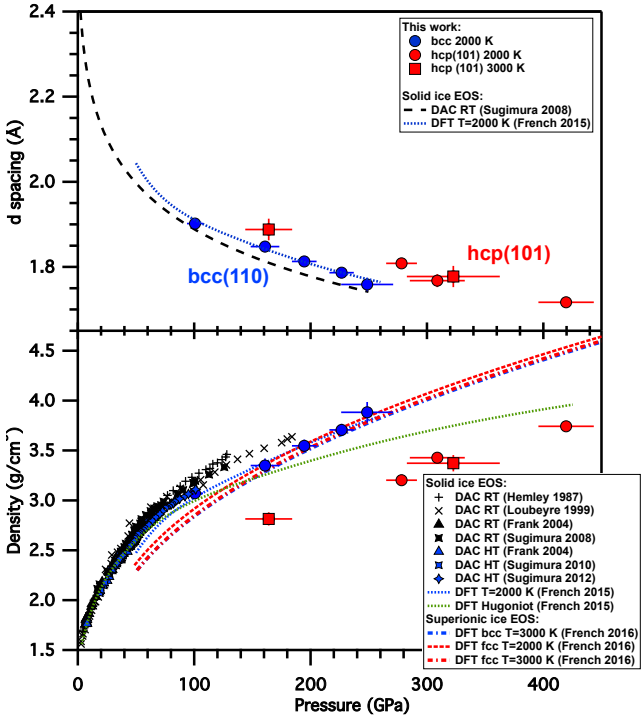

Supplementary Figure 9. **d-spacing and density vs pressure assuming the diffraction peak observed above 270 GPa is *hcp* (101) for an hexagonal closed packed lattice of oxygens**. Red circles and squares represent the density of water ice assuming high pressure phase has a *hcp* lattice of oxygens, fitting the measured d-spacing to the *hcp* (101) reflection. This would imply a huge density drop that would also bring the ice density below the density of *bcc* ice along the ice VII Hugoniot (green dotted curve), which is clearly unphysical.

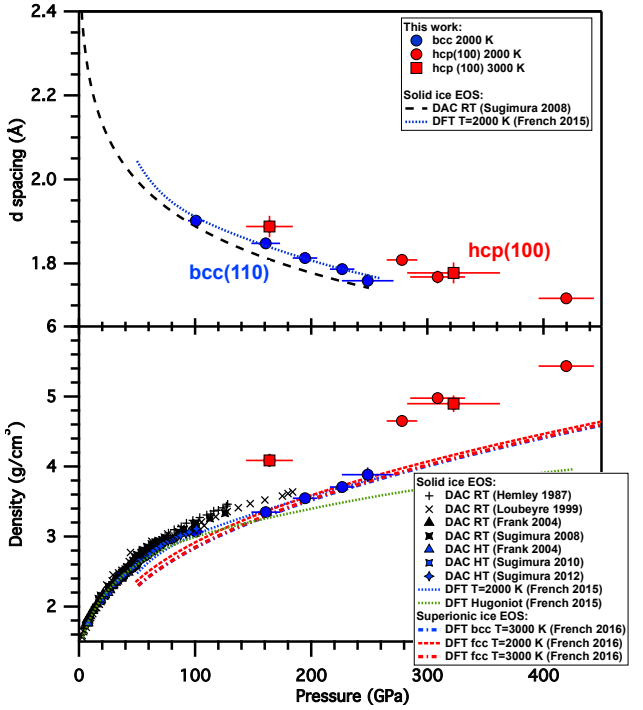

Supplementary Figure 10. **d-spacing and density vs pressure assuming the diffraction peak observed above 270 GPa is *hcp* (100) for an hexagonal closed packed lattice of oxygens**. Red circles and squares represent the density of water ice if the high pressure phase has a *hcp* lattice of oxygens, fitting the measured d-spacing to the *hcp* (100) reflection. The calculated density is higher than the initial density of bcc water ice at 300 K, which is unphysical for high temperature data.

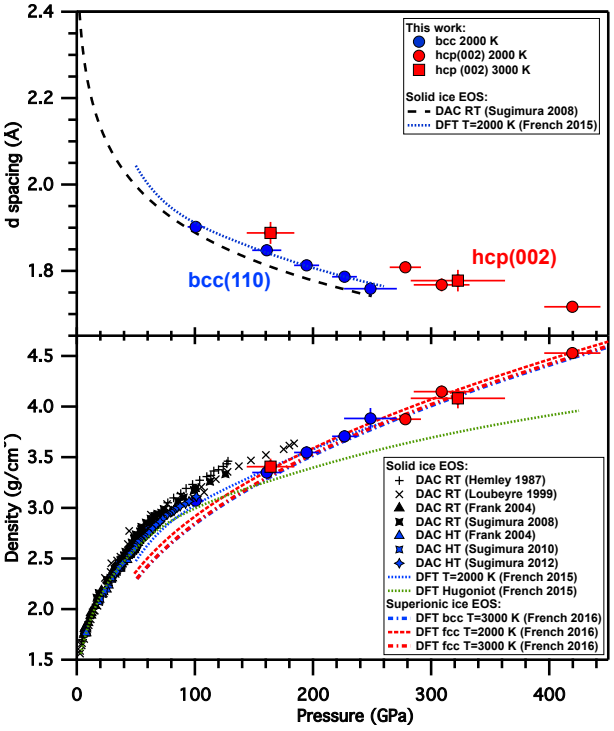

Supplementary Figure 11. **d-spacing and density vs pressure assuming the diffraction peak observed above 270 GPa is *hcp*(002) for an hexagonal closed packed lattice of oxygens**. Red circles and squares represent the density of water ice if high pressure phase has a *hcp* lattice of oxygens, fitting the measured d-spacing to the *hcp*(002) reflection. The calculated density in this case is consistent with the expected stress-density response of water.

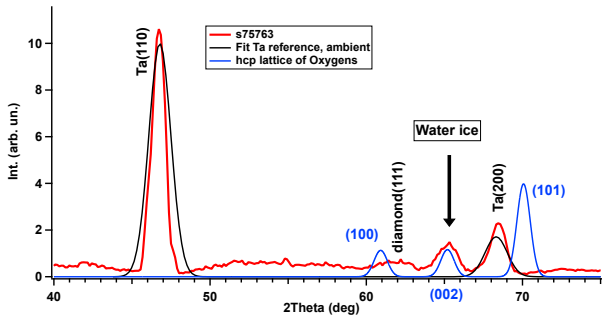

Supplementary Figure 12. **Comparison of the experimental diffraction pattern measured at 420 GPa and 2,000 K with the *hcp* lattice of oxygens, assuming the observed peak is the (002) reflection**. Red pattern is the diffraction signal measured in shot 75763, compared with the diffraction pattern for ambient conditions Ta (reference pinhole material) in black and the expected signal for an *hcp* lattice of oxygens with the (002) reflection matching the position of the observed signal from water (blue curve). Given the relative spacing of the triplet characteristic of the *hcp* lattice with c/a=1.63 one would have expected to observe the (101) reflection as well. A different c/a will change the relative spacing between the (002) and the (101) reflection, however there is no value that will allow to fit the peaks assigned to water ice and the one assigned to Ta(200) (assuming overlap) simultaneously.

C. X-ray diffraction signal related to the diamond ablator and window

While single crystal diamonds are chosen as the ablator and window to minimize their contribution to the diffraction signal, they still produce intense, localized diffraction features in almost all the shots (see Supplementary Figure 5 and Supplementary Figure 6).

To illustrate in more details the density distribution within the diamond ablator and window during the x-ray flash, we show the space-time contour map and distribution histograms in Supplementary Figure 13.

It appears clearly that the portion of the ablator that is not ablated away is significantly compressed and in a rather uniform state at 11 ns when the x-rays are generated. In this particular shot 75758, the simulation shows that the density distribution peaks at $4.31 \pm 0.04\ g/cm^3$. This corresponds to a d-spacing of 1.926 ± 0.006Å for the (111) (most intense) reflection of diamond. In the same shot the d-spacing corresponding to the signal assigned to the water ice is 1.813 ± 0.011 Å.

On the other hand, the diamond window is bounded by vacuum on one side, and has not reached peak compression at the time of the x-ray probe. Most of the diamond window is therefore at lower density than the ablator, close to ambient conditions. In this particular run, Fig Supplementary Figure 13 (c) indicates that the broad density distribution is dominated by the double-shock state near 3.7 g/cm^3, which corresponds to $\sim 6\%$ compression and a d-spacing of 2.03 Å for the (111) reflection of diamond.

This makes a first compelling case that there is no ambiguity between the diffraction signal originating from diamond (both ablator and window) and from the water ice. A second strong observation supporting our assignment is related to the loss of the single crystal nature of compressed diamonds. Indeed, the rapid strong compression transforms the diamonds into highly textured polycrystals. This is apparent in the x-ray diffraction signal shown in Figure 3, Supplementary Figure 5 and Supplementary Figure 6. In the majority of the shots, we observe an azimuthally-localized, oval-shaped strong spot that appears at a 2θ angle slightly lower than the Bragg angle for the signal originating from the water ice. This is evident in the dewarped data shown for shots # 75763 and 75761 in Figure 3, as well as the data for shots # 74700, 75758, 75760 and 75762 shown in Supplementary Figure 5 and Supplementary Figure 6

This is perhaps easier to grasp in the raw image plate data shown in Supplementary Figure 14 where one can clearly distinguish the difference in the XRD signal between the small-grained water ice (indicated by a red arrow in panel (a)) and the highly textured diamond (black arrows in panels (a) and (c)). We should stress that the location of the diamond diffraction signal along the ring (i.e. the azimuthal angle) is random, since the clocking of the diamond ablators and windows are not controlled during the target assembly. This explains the variation in the ϕ angle corresponding to the diamond peak

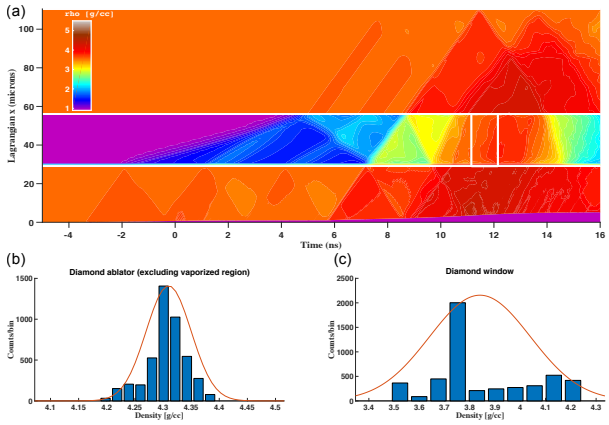

Supplementary Figure 13. **Compression of the diamond ablator and window**. **(a)** Density map corresponding to Figure 3. **(b)** and **(c)** Histograms of the density distribution in the diamond ablator and window during the x-ray flash. For clarity we excluded the region ablated away ($x < 5\ \mu m$, shown in magenta in **(a)**) from the statistical analysis.

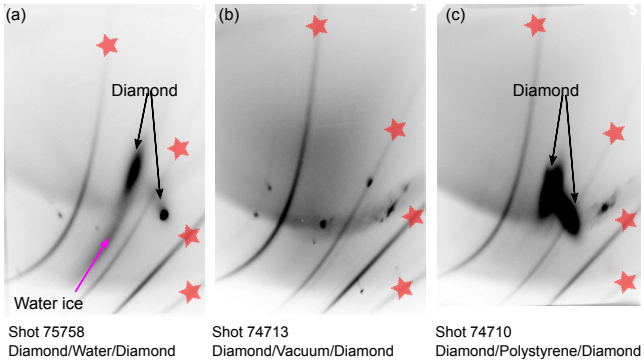

Supplementary Figure 14. **Control experiments.** Raw image plate data for **(a)** shot 75758 (standard water sample) and two control experiments: **(b)** shot 74713 with a vacuum gap to replace the water layer and **(c)** shot 74710 with a polystyrene surrogate. The three shots used the same nominal laser pulse shape and energy. In the three experiments the diffraction signal from the Ta collimating aperture is indicated by red stars, while the arrows point to the diffraction signal from diamond (black) and from the water ice (magenta). It is clear that the signal we assign to water ice (rather smooth and azimuthally extended) is present only in the shot containing a water sample.

seen in different experiments (as shown in Supplementary Figure 5 and Supplementary Figure 6) and also why no diamond peak is seen in the image plate in Supplementary Figure 14(b).

In addition, the laser drive pulse shape has been designed to achieve – at the x-ray probe time – a uniform pressure state in the water layer, but not in the diamonds (as shown by the density map and distributions in Supplementary Figure 13). The signal from diamond can therefore extend over a broad 2θ range corresponding to the different pressure (or density) states during the x-ray flash. This is the case for shot 74710 shown in Supplementary Figure 14 where the brightest spots assigned to diamond show a large 2θ extension.

Finally, it is worth noting, that similar signatures for the diamonds have been consistently observed in a quite broad spectrum of experiments on different materials carried out with the PXRDIP diagnostic at the Omega Laser and reported in Refs.[18,19,46–48].

D. Control experiments with a polystyrene surrogate

We performed control experiments to gain further confidence in our interpretation of the diffraction from the water ices.

Control experiments need to reproduce as much as possible the water experiments. Because the initial density and compressibility of the water sample are the main factors (together with the laser pulse shape and the target thickness) determining the compression history in both the diamond ablator and window, we choose to use $30\mu m$ polystyrene foils with an initial density of 1.05 g/cm^3 as a surrogate for the water layer. The compressibility of polystyrene under single-and multi-shock compression is indeed quite similar to that of water (see Supplementary Figure 15 and Refs.[49,50]).

In shot 74710 we compress a diamond/polystyrene/diamond target with the same pulse shape and laser energy as the water target in shot 75758. Given the similarity between water and polystyrene, the compression history is very similar in the two cases. In Supplementary Figure 14 we compare the raw diffraction images for shot 75758 (water target, (a)) and shot 74710 (polystyrene target, (c)). As can be observed, the diffraction signal characteristic of the diamond (very intense and of limited azimuthal extension) is present in both shots (black arrows), but the more azimuthally-extended and weaker diffraction signal (magenta arrow) is not, providing another additional piece of evidence in support of the assignment of this signal as due to the crystallization of water.

We also report the results of an experiment with a target having a 30 μm vacuum gap between the two diamonds. Although the vacuum causes the compression history of the ablator and window to be quite different from the case of a water target, no XRD signatures similar to the one we interpret as arising from the H_2O ices (in the experiments with water-filled targets) are present in this shot (see panel (b) of Supplementary Figure 14).

S6. CONSTRAINTS ON THE KINETICS OF SOLIDIFICATION AND GRAIN GROWTH

Without observing multiple XRD lines for the ice crystal lattice, we cannot perform a Warren-Averbach analysis to formally identify the respective contributions of strain and grain size to the angular broadening that we observe[51]. However, at the high temperatures that we explored experimentally, we argue that it is reasonable to assume that ice is soft enough so that the strain distribution should reflect the imposed stress

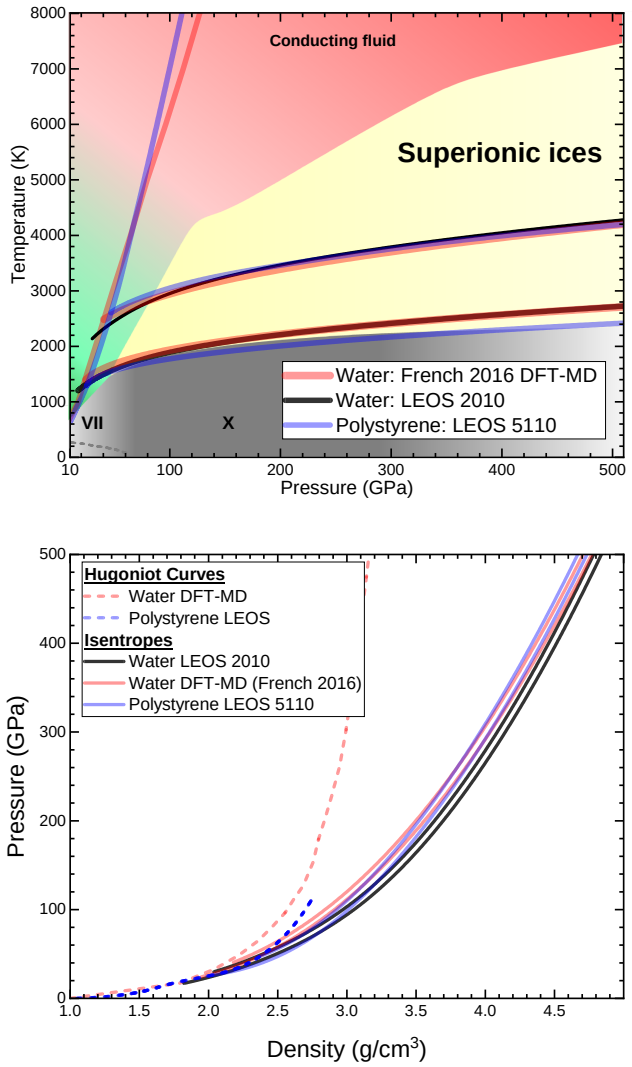

Supplementary Figure 15. **Compressibility of water and polystyrene. (Top)** Pressure-temperature phase diagram for water with boundaries from Ref.[11]. The Hugoniot and two shock-ramp isentropic compression paths relevant for the present study and calculated with the LEOS 2010 table and the DFT-MD based equation of state model from[15] are shown. Also shown are similar curves for polystyrene used as surrogate in the control experiment shot 74710 (see Supplementary Figure 14). **(Bottom)** Corresponding curves in the pressure-density space. In the region of the phase diagram investigated in this work LEOS 2010 matches very well the prediction from state of the art DFT-MD models[15,27], given the similar pressure-density response.

non-uniformity. In other words, we expect that there is a larger strain inhomogeneity within the ice sample in the experiments for which we estimate that the stress-inhomogeneity is the largest from the statistical analysis of the hydrodynamic simulation results. If the variations of strain within the sample during the x-ray exposure were the dominant source of angular broadening for the ice peak, we would therefore expect to observe broader peaks for the experiments with the largest stress-inhomogeneity. However, the top panel of Supplementary Figure 16 does not reveal such a trend: the FWHM of the ice peak (solid circles) does not seem to significantly increase with increasing pressure inhomogeneity.

In contrast, the bottom panel of Supplementary Figure 16 may suggest that the FWHM of the ice peak decreases with increasing growth time delay Δt, where Δt is defined as the delay between the instant H_2O is brought below the melting line, *i.e.* into the predicted stability field of ice, and the time of the XRD snapshot (see Figure 2b). This is the expected behavior if grain size effects dominate the XRD angular broadening: longer growth delay allow larger grain to grow, reducing the angular broadening of the XRD peaks.

In the following we assume that grain size is the main contribution for the observed diffraction peak broadening. This is justified because we estimate the contribution from other effects, such as the experimental resolution, to be about 0.8 degree and the pressure gradient component (see Supplementary Information Section S4) to be around 1 degree (see open diamonds in Supplementary Figure 16).

Based on these observations, we use the Scherrer equation to infer a minimum grain size for the ice crystals from the measured FWHM which reveals grain sizes around 5 nm in diameter (Supplementary Information Section S4). Clearly, deconvolving the resolution and strain component from the total FWHM before using the Scherrer equation would produce slightly larger (~ 2 times bigger) values for the minimal grain size.

We also plot the inferred minimum grain size against the growth delay time Δt for all our experiments on Supplementary Figure 17. Because in the Scherrer equation the minimum grain size is inversely proportional to the angular broadening, the data in Supplementary Figure 17 are closely related to the bottom panel of Supplementary Figure 16 and may suggest larger grain sizes at longer growth time delay.

There is a large number of models for the kinetics of freezing and grain growth[25,52–55]. A simple picture of nucleation and growth of spherical particles out of a liquid suggests that after an incubation/nucleation time τ, the grain size should increase with time[24,54,56] as: $D = k(\Delta t - \tau)^{(1/n)}$ where the exponent $1/n$ is determined by the grain growth mechanism. In this framework[54], initial explosive growth leads to $n = 1$ while $n \geq 3$ is expected for grain growth by competitive capture and coalescence. For example, recent billion-atom MD simulations of the sub-nanosecond solidification of an undercooled iron melt[25] suggest that grain growth by coalescence leads to $D \propto (\Delta t - \tau)^{1/n}$ with $n \approx 6$, while other simulations on the crystallization of fused silica under shock compression indicate $n \simeq 3$ for the coalescence phase[54].

The data shown on Supplementary Figure 17 provide an upper bound for the nucleation time $\tau \sim$1-2 ns.

However, our data does not allow us to unambiguously identify the nucleation and growth mechanism in our experiments: as it appears on Supplementary Figure 17, the green and magenta fits to the data using $n = 3$ or $n = 6$ give statistically equivalent results, and dedicated experiments are necessary to provide more quantitative tests for kinetic models of crystallization.

We also cannot identify a statistically significant difference

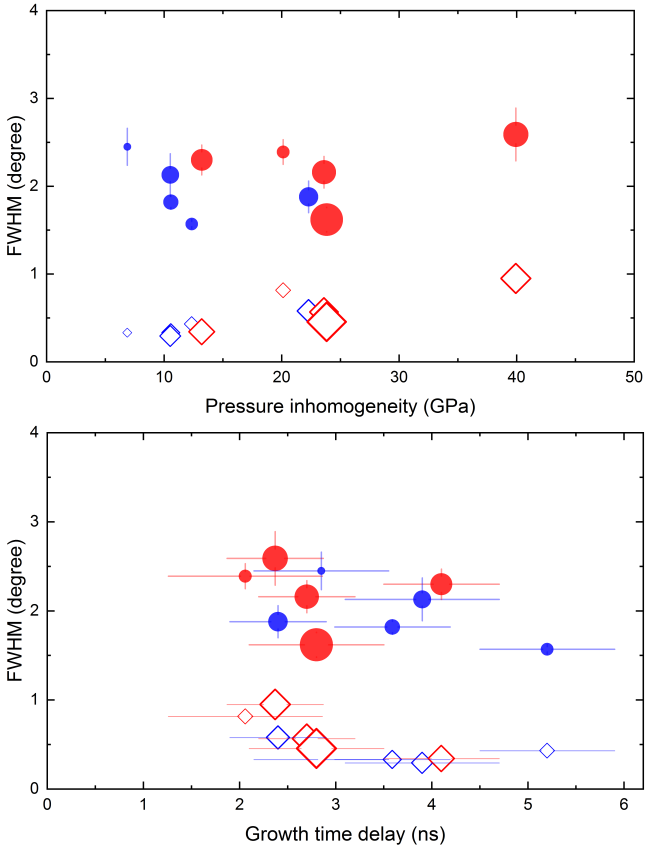

Supplementary Figure 16. **Angular broadening of the H_2O XRD peak.** Solid symbols: total measured full-width at half maximum (FWHM), open symbols: estimated contribution from the pressure inhomogeneity. The symbol size in both panels is proportional to the pressure for each data point. The color is associated with the structure with *bcc* in blue and *fcc* in red. (**Top**) FWHM plotted as a function of the pressure inhomogeneity inferred from the statistical analysis of the hydrodynamic simulation results. (**Bottom**) FWHM plotted as a function of the growth time delay Δt extracted from the hydrodynamics simulations and defined as the delay between the instant H_2O is brought below the melting line, *i.e.* into the predicted stability field of ice, and the time of the XRD snapshot (see Figure 2b).

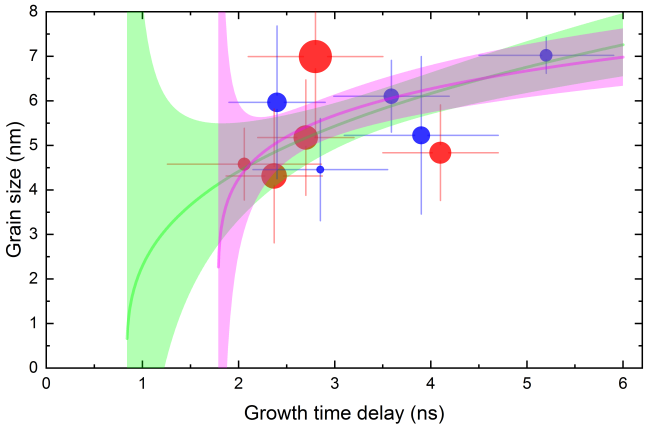

Supplementary Figure 17. **Kinetics of solidification and growth.** Estimated minimum grain size D – inferred from the width of the XRD peaks – as a function of the growth time delay Δt extracted from the hydrodynamics simulations and defined as the delay between the instant H_2O is brought below the melting line, *i.e.* into the predicted stability field of ice and the time of the XRD snapshot (see Figure 2b). *bcc* points are in blue, *fcc* in red and the size of the symbol is proportional to the peak pressure. Colored lines represent fits to the data assuming $D = k(\Delta t - \tau)^{(1/n)}$ with $n = 3$ (green) and $n = 6$ (magenta). Shaded areas represent 95% confidence bands for these fits.

in kinetics mechanism between the data for superionic and insulating ice (*i.e.* between the blue and red points) which may suggest that nucleation and growth mechanisms are similar for the two phases.

S7. PREVIOUS STUDIES OF WATER ICE AT HIGH PRESSURE

In Supplementary Figure 18 and Supplementary Figure 19 we show the pressure-temperature conditions and the corresponding pressure-density data obtained in previous x-ray diffraction studies of water ice in the diamond anvil cell (DAC). Given the challenges of measuring diffraction of such a low scattering system at extreme P-T conditions in the diamond anvil cell, only one or two diffraction peaks are observed in most studies.

Hemley *et al.,* (orange right-pointing triangles) used energy dispersive XRD to measure[33] the room temperature compression curve of a polycrystalline sample up to 128 GPa with ruby as the pressure reference.

Loubeyre *et al,.* (gray squares) performed single-crystal angular dispersive XRD at room temperature, using Au as the pressure reference. The experimental pressures revised by the authors are reported in Ref.[16] using an improved Au scale[57] yielding a maximum pressure of 184 GPa.

Frank *et al.,* (cyan diamonds) performed[35] energy dispersive XRD in an externally heated DAC with Au as an internal pressure calibrant up to 65 GPa and up to 900 K. Melting is determined up to 37 GPa and 850 K and the highest P-T points that fall in the white shaded area in Supplementary Figure 18 are in the liquid phase.

Sugimura *et al.,* (purple down-pointing triangles) performed[26] angular dispersive XRD at room temperature up to 126 GPa using Pt as an internal pressure calibrant, or the secondary pressure scale based on the diamond anvil Raman signal.

A second report[36] by Sugimura *et al.,* (pink left-pointing triangles) describes high temperature EOS measurements using angular dispersive XRD in an externally heated DAC with Au and Pt as internal pressure calibrants up to 50 GPa at 900 K.

A third report[37] by Sugimura *et al.,* (green up-pointing triangles) on electrical conductivity measurements of ice includes high temperature EOS measurements using angular dispersive XRD in an externally heated DAC with Au and Pt as internal pressure calibrants up to 100 GPa along the 900 K

isotherm.

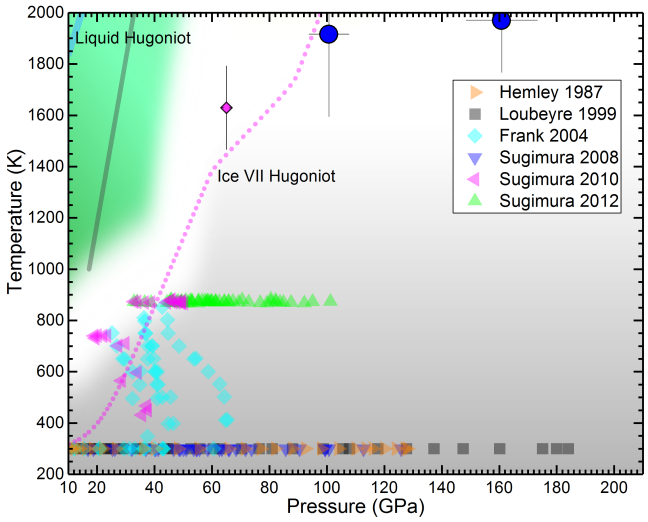

Supplementary Figure 18. **Phase diagram of H_2O below 200 GPa and 2,000 K.** Calculated Pressure - Temperature conditions for our data below 200 GPa (blue circles) are shown together with the measured P-T conditions for previous XRD experiments using diamond anvil cells by Hemley *et al.,*[33], Loubeyre *et al.,*[34] Frank *et al.,*[35] and Sugimura *et al.,*[26,36,37]. Pink dotted line is the ice VII Hugoniot curve calculated in Ref.[16] and the pink diamond corresponds to the lowest pressure electrical conductivity measurements in Chau *et al.,*[21].

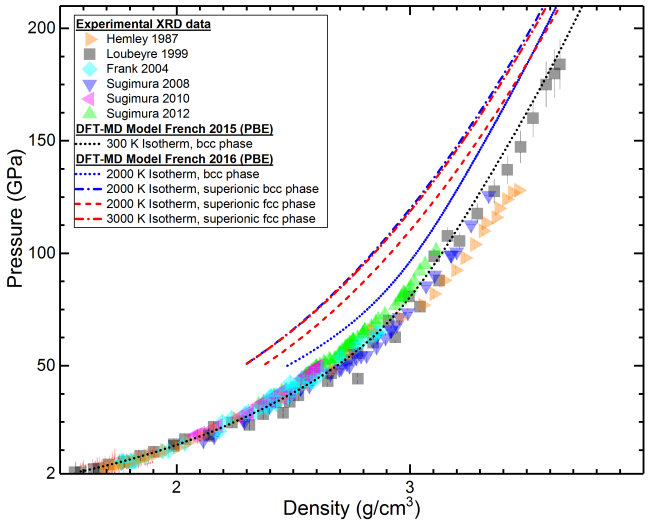

Supplementary Figure 19. **Pressure-density of H_2O ice obtained by XRD.** Previous XRD experiments using diamond anvil cells by Hemley *et al.,*[33], Loubeyre *et al.,*[34] Frank *et al.,*[35] and Sugimura *et al.,*[26,36,37]. Isotherms calculated with the DFT-MD models from French *et al.,*[15,27] as shown in Figure 3.

Many simulation studies have investigated the properties and phase boundaries of superionic water ices[6–15,28,58–62].

Several studies using the density-functional-theory (DFT) investigated the fate of ice to ultrahigh pressure beyond the experimentally explored range and proposed that[28,30,31,63–65]

Supplementary Table 1. **Most recently discovered phases of water ice.** Adapted from *http://www1.lsbu.ac.uk/water/ice_phases.html*

Phase	Notes	Reference
Ice XIII	Proton ordered counterpart of ice V	Salzmann 2007 [68]
Ice XIV	Proton ordered counterpart of ice XII	Salzmann 2007 [68]
Ice XV	Proton ordered counterpart of ice VI	Salzmann 2009 [69,70]
Ice XVI	Empty clathrate	Falenty 2014 [71]
Ice XVII	Porous phase	DelRosso 2016 [17]
Ice XVIII	Superionic *fcc*	This work

H_2O adopts a series of increasingly distorted and complex structures with a $Pbcm$ phase above 300 GPa[28] (at 0 K), $Pbca$ near 760 GPa[30], $P3_121$ near 780 GPa[63], $Pcca$ near 1,400 GPa[63] and $P2_1/c$ near 2,000 GPa[65]. Metallization is predicted at the transition into $C2/m$ phase above 6,000 GPa[64,66] but water might dissociate into H_2O_2 near 5,000 GPa[63] or H_4O near 1,400 GPa[67].

We compiled a brief summary of the ice phases that have been recently discovered in Supplementary Table 1.

S8. NUMERICAL SIMULATIONS OF THE ELASTIC PROPERTIES OF SUPERIONIC WATER ICE

We use Density Functional Theory Molecular Dynamics (DFT-MD also known as QMD) to calculate the finite-temperature elastic constants of superionic water from which we can obtain the shear modulus.

We follow the methodology of Refs.[12,72] and perform a series of QMD simulations in the canonical ensemble (NVT) with small deformation of the simulation cells in order to extract the stress-strain relationship by finite difference for this system at pressures relevant to the interior of planets.

The deformation of the simulation cell A is taken to be $A' = A(1+\epsilon)$ where:

$$\epsilon = \begin{pmatrix} e & 0 & 0 \\ 0 & 0 & e/2 \\ 0 & e/2 & 0 \end{pmatrix}$$

and where e is a small number (we use $e = \pm\, 0.01$).

For cubic systems, this deformation allows for a straightforward evaluation of the elastic constants.

A. Stress-strain relations

General stress-strain relations for a linear elastic material can be cast as:

$$\begin{pmatrix} \sigma_{11} \\ \sigma_{22} \\ \sigma_{33} \\ \sigma_{23} \\ \sigma_{13} \\ \sigma_{12} \end{pmatrix} = \begin{pmatrix} C_{1111} & C_{1122} & C_{1133} & C_{1123} & C_{1113} & C_{1112} \\ & C_{2222} & C_{2233} & C_{2223} & C_{2213} & C_{2212} \\ & & C_{3333} & C_{3323} & C_{3313} & C_{3312} \\ & & & C_{2323} & C_{2313} & C_{2312} \\ & symm & & & C_{1313} & C_{1312} \\ & & & & & C_{1312} \end{pmatrix} \begin{pmatrix} \epsilon_{11} \\ \epsilon_{22} \\ \epsilon_{33} \\ \epsilon_{23} \\ \epsilon_{13} \\ \epsilon_{12} \end{pmatrix}$$

where the symmetric 3×3 stress matrix σ is expressed as a vector. The tensor notation is simplified by giving indices to all the components:

$$\begin{pmatrix} \sigma_1 \\ \sigma_2 \\ \sigma_3 \\ \sigma_4 \\ \sigma_5 \\ \sigma_6 \end{pmatrix} = \begin{pmatrix} C_{11} & C_{12} & C_{13} & C_{14} & C_{15} & C_{16} \\ & C_{22} & C_{23} & C_{24} & C_{25} & C_{26} \\ & & C_{33} & C_{34} & C_{35} & C_{36} \\ & & & C_{44} & C_{45} & C_{46} \\ & symm & & & C_{55} & C_{56} \\ & & & & & C_{66} \end{pmatrix} \begin{pmatrix} \epsilon_1 \\ \epsilon_2 \\ \epsilon_3 \\ \epsilon_4 \\ \epsilon_5 \\ \epsilon_6 \end{pmatrix}$$

To be clear, a general deformation (strain) is:

$$\begin{pmatrix} \epsilon_{11} & \epsilon_{12} & \epsilon_{13} \\ & \epsilon_{22} & \epsilon_{23} \\ & & \epsilon_{33} \end{pmatrix} \rightarrow \begin{pmatrix} \epsilon_{11} \\ \epsilon_{22} \\ \epsilon_{33} \\ 2\epsilon_{23} \\ 2\epsilon_{13} \\ 2\epsilon_{12} \end{pmatrix} \rightarrow \begin{pmatrix} \epsilon_1 \\ \epsilon_2 \\ \epsilon_3 \\ \epsilon_4 \\ \epsilon_5 \\ \epsilon_6 \end{pmatrix}$$

and our particular deformation is then:

$$\epsilon = \begin{pmatrix} e & 0 & 0 \\ 0 & 0 & e/2 \\ 0 & e/2 & 0 \end{pmatrix} \rightarrow \begin{pmatrix} e & 0 & 0 \\ & 0 & e/2 \\ & & 0 \end{pmatrix} \rightarrow \begin{pmatrix} e \\ 0 \\ 0 \\ e \\ 0 \\ 0 \end{pmatrix} = \begin{pmatrix} \epsilon_1 \\ \epsilon_2 \\ \epsilon_3 \\ \epsilon_4 \\ \epsilon_5 \\ \epsilon_6 \end{pmatrix}$$

For a cubic system $C_{12} = C_{13}$, $C_{11} = C_{22} = C_{33}$, $C_{44} = C_{55} = C_{66}$ and the rest are 0 by symmetry. The stress-strain relations reduce to:

$$\begin{pmatrix} \sigma_{11} \\ \sigma_{22} \\ \sigma_{33} \\ \sigma_{23} \\ \sigma_{13} \\ \sigma_{12} \end{pmatrix} = \begin{pmatrix} \sigma_1 \\ \sigma_2 \\ \sigma_3 \\ \sigma_4 \\ \sigma_5 \\ \sigma_6 \end{pmatrix} = \begin{pmatrix} C_{11} & C_{12} & C_{12} & 0 & 0 & 0 \\ C_{12} & C_{11} & C_{12} & 0 & 0 & 0 \\ C_{12} & C_{12} & C_{11} & 0 & 0 & 0 \\ 0 & 0 & 0 & C_{44} & 0 & 0 \\ 0 & 0 & 0 & 0 & C_{44} & 0 \\ 0 & 0 & 0 & 0 & 0 & C_{44} \end{pmatrix} \begin{pmatrix} e \\ 0 \\ 0 \\ e \\ 0 \\ 0 \end{pmatrix}$$

or:

$$C_{11} = \sigma_{11}/e \quad (1)$$
$$C_{12} = \sigma_{22}/e \quad (2)$$
$$C_{12} = \sigma_{33}/e \quad (3)$$
$$C_{44} = \sigma_{23}/e \quad (4)$$

B. Computational Details

Our QMD simulations are carried out with the Vienna *ab-initio* Simulation Package[73] with projector augmented wave (PAW) pseudopotentials[74,75]. We use Born-Oppenheimer Molecular dynamics within the NVT ensemble with Nosé-Hoover thermostat[76,77] with a MD time step of 0.4 fs. We use PAW with core radii of 0.8 Bohr for hydrogen and 1.1 Bohr for oxygen and the generalized gradient approximation (GGA) of DFT with the Perdew-Burke-Ernzerhof (PBE) exchange-correlation functional[78]. The plane-wave cutoff is set to 1000 eV. The electronic density is constructed from a single-particle wave function by sampling at the Γ point of the Brillouin zone and using Fermi smearing according to the average ionic temperature. Simulation cell sizes are 324 atoms.

The various stress components needed to evaluate Eq. 1- 4 are averaged over the MD trajectory. Supplementary Figure 20 illustrates the time variation of the stress components for superionic water ice at 4.25 g/cm^3 and 4,000 K while Supplementary Figure 21 shows the same for the $e = -0.01$ distortion for the σ_1, σ_2, σ_3 and σ_4, σ_5, σ_6 in separate plots. Supplementary Figure 22 shows how much the value of the average stress varies with the length of the MD trajectory over which that average is taken. These average values are then collected and plotted as a function of the strain on the cell (see Supplementary Figure 23). We note that a linear fit for the various stress-strain relations appears to be sufficient given the small distortion used. The slope of this function is then the elastic constant according to Eq. 1- 4.

C. Bulk and shear moduli

The single-crystal isothermal bulk modulus $K = \frac{C_{11}+2C_{12}}{3}$, the tetragonal shear $C_s = \frac{C_{11}-C_{12}}{2}$ and the shear C_{44} along the 4000 K isotherm are shown in Supplementary Figure 24.

For cubic polycrystals, the average isotropic shear modulus is determined from single-crystal elastic moduli according to the Voigt-Reuss-Hill scheme (the arithmetic average between a lower bound and a higher bound). In the cubic case, this reduces to[79]:

$$G_V = \frac{1}{5}(2C_s + 3C_{44})$$
$$G_R = \left[\frac{1}{5}(\frac{2}{C_s} + \frac{3}{C_{44}})\right]^{-1}$$
$$G_H = \frac{1}{2}(G_V + G_R)$$

while for face-centered or body-centered cubic crystals the average bulk modulus is:

$$K_H = K_R = K_V = \frac{C_{11} + 2C_{12}}{3}$$

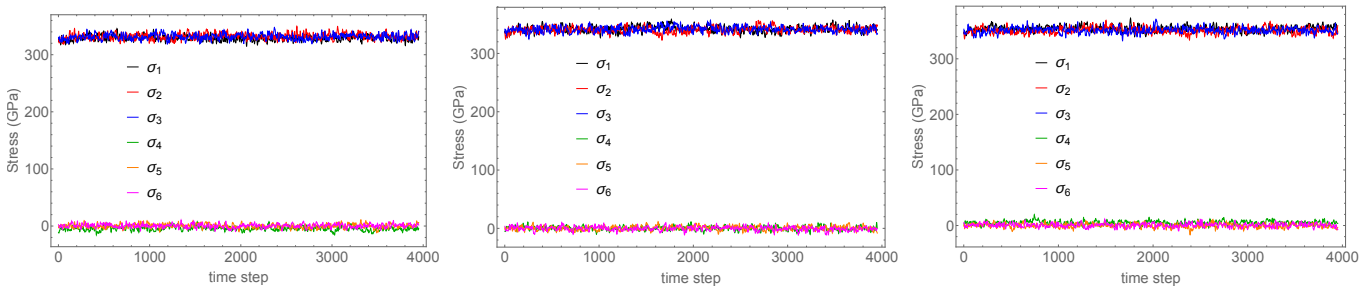

Supplementary Figure 20. **MD simulation results.** Stress vs MD time step for different distortions of the MD supercell: e=0.01 (**Left**), e=0 (**Center**), e=-0.01 (**Right**).

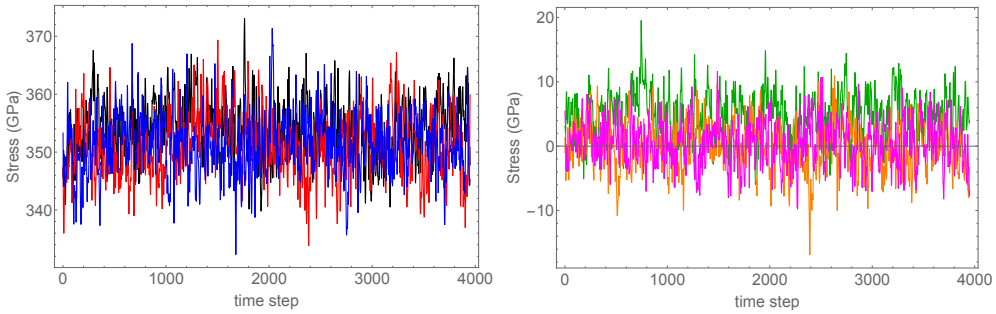

Supplementary Figure 21. **MD simulation results.** Stress versus MD time step for the e=-0.01 distortions of the MD supercell: σ_1 in black, σ_2 in red, σ_3 in blue (**Left**), σ_4 in green, σ_5 in orange, σ_6 in magenta (**Right**).

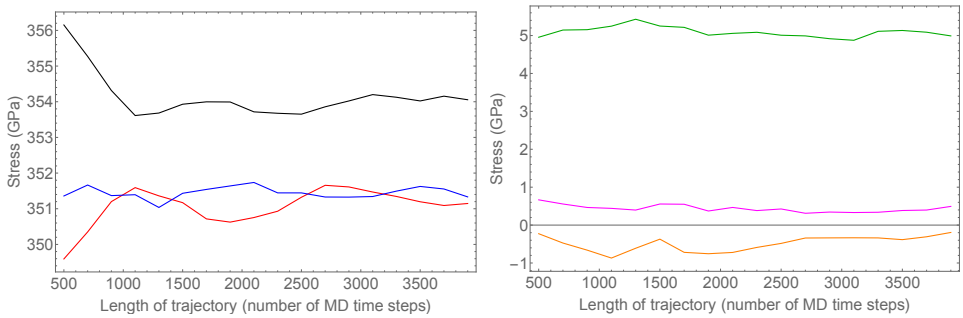

Supplementary Figure 22. **MD simulation results.** Average stress versus number of MD time steps for the e=-0.01 distortions of the MD supercell: σ_1 in black, σ_2 in red, σ_3 in blue (**Left**), σ_4 in green, σ_5 in orange, σ_6 in magenta (**Right**).

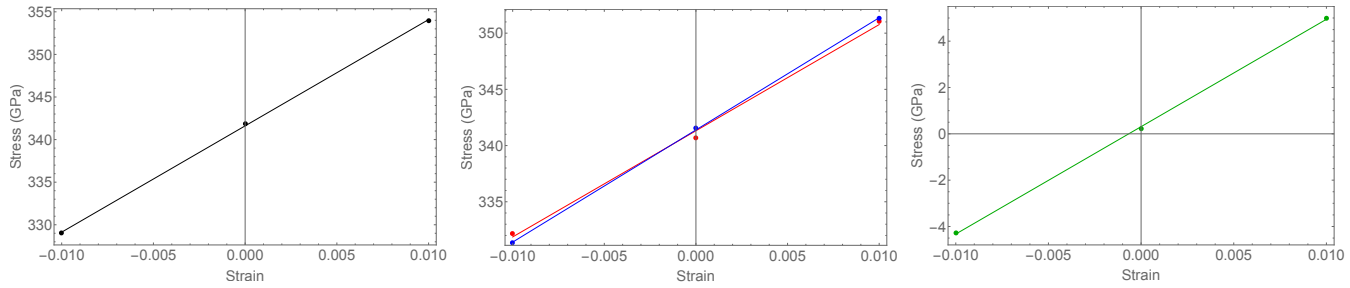

Supplementary Figure 23. **MD simulation results.** Average stress vs strain. σ_1 in black, the slope of which gives C_{11} (**Left**), σ_2 in red, σ_3 in blue, we take the average of the slopes to get C_{12} (**Center**), σ_4 in green, the slope of which gives C_{44} (**Right**).

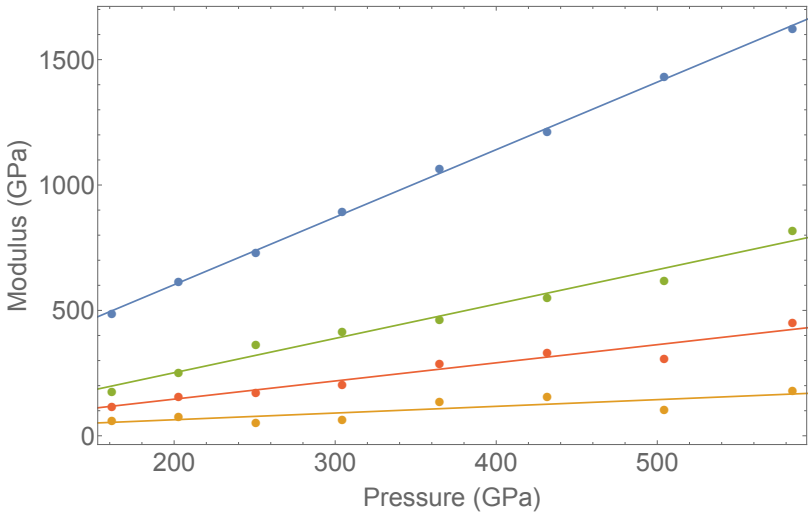

Supplementary Figure 24. **Elastic moduli computed with DFT-MD**. Pressure dependence of the elastic moduli of *fcc* superionic water ice along the 4000 K isotherm. Isothermal bulk modulus $K = K_H$ (blue). Single-crystal shear modulus C_{44} (green). Poly-crystal Voigt-Reuss-Hill averaged shear modulus $G = G_H$ (red). Single-crystal tetragonal shear modulus C_s (orange). Lines are fits whose parameters are: $K = 63.9 + 2.69P$, $C_s = 10.5 + 0.267P$, $C_{44} = -22.6 + 1.37P$ and $G_H = 2.21 + 140/(3.87 - P) + 0.723P$ (with P in GPa).

Supplementary Table 2. **Experimental details and results.** Diamond ablator, window and water layer thickness. Measured d-spacing, full-width at half maximum (FWHM) of the Bragg peaks and estimated contribution of the distribution of compression states to the angular broadening $\Delta 2\theta_{Inhom}$. Density, pressure and temperature for each shot, as well as inferred phase, timing of the beginning of the 1-ns long x-ray source (XRS) pulse and the growth time delay Δt (time difference between the water entering the superionic ice stability field and the x-ray snapshot).

Shot ID	Ablator μm	Sample μm	Window μm	d-spacing Å	FWHM degree	$\Delta 2\theta_{Inhom}$ degree	Density g/cm^3	Pressure GPa	Temperature K	Phase	XRS ns	Δt ns
73144	18.5	30	102	1.902 ± 0.011	2.45 ± 0.21	0.33	3.072 ± 0.054	101 ± 7	1920 ± 320	bcc	9.65	2.9
74700	36	30	56	1.848 ± 0.013	1.57 ± 0.03	0.43	3.349 ± 0.072	161 ± 12	1970 ± 200	bcc	13.2	5.2
75758	29	30	54.5	1.813 ± 0.011	1.82 ± 0.08	0.33	3.547 ± 0.063	195 ± 11	2230 ± 280	bcc	11.15	3.6
73149	26.5	30	89	1.787 ± 0.010	2.13 ± 0.24	0.29	3.707 ± 0.062	227 ± 11	2250 ± 350	bcc	11.7	3.9
75761	35	30	49	1.759 ± 0.016	1.88 ± 0.18	0.58	3.883 ± 0.104	249 ± 22	1670 ± 100	bcc	11.7	2.4
73146	26.5	30	96	1.809 ± 0.011	2.30 ± 0.17	0.34	3.890 ± 0.069	278 ± 13	2340 ± 390	fcc	11.7	4.1
75759	30.5	30	61	1.768 ± 0.015	2.16 ± 0.18	0.57	4.164 ± 0.108	309 ± 24	2380 ± 370	fcc	7.7	2.7
75763	32	30	59.5	1.717 ± 0.012	1.62 ± 0.14	0.46	4.546 ± 0.092	420 ± 24	2680 ± 320	fcc	10.6	2.8
75762	29	30	60	1.888 ± 0.025	2.39 ± 0.14	0.82	3.419 ± 0.138	164 ± 20	3230 ± 480	fcc	7.16	2.1
75760	25	30	53.5	1.778 ± 0.025	2.59 ± 0.30	0.95	4.097 ± 0.172	323 ± 40	3800 ± 650	fcc	7.17	2.4

S9. REFERENCES

[1] Bridgman, P. Water, in the Liquid and Five Solid Forms, under Pressure. *Proc. Am. Acad. Arts Sci.* **47**, 441–558 (1912).

[2] Bartels-Rausch, T. *et al.* Ice structures, patterns, and processes: A view across the icefields. *Rev. Mod. Phys.* **84**, 885–944 (2012).

[3] Malenkov, G. Liquid water and ices: understanding the structure and physical properties. *J. Phys. Condens. Matter* **21**, 283101 (2009).

[4] Pallares, G. *et al.* Anomalies in bulk supercooled water at negative pressure. *Proc. Natl. Acad. Sci. U. S. A.* **111**, 7936–41 (2014).

[5] Mishima, O. & Stanley, H. E. The relationship between liquid, supercooled and glassy water. *Nature* **396**, 329–335 (1998).

[6] Demontis, P., LeSar, R. & Klein, M. L. New high-pressure phases of ice. *Phys. Rev. Lett.* **60**, 2284–2287 (1988).

[7] Cavazzoni, C. *et al.* Superionic and Metallic States of Water and Ammonia at Giant Planet Conditions. *Science (80-.).* **283**, 44–46 (1999).

[8] Mattsson, T. R. & Desjarlais, M. P. Phase diagram and electrical conductivity of high energy-density water from density functional theory. *Phys. Rev. Lett.* **97**, 1–4 (2006).

[9] Schwegler, E., Sharma, M., Gygi, F. & Galli, G. Melting of ice under pressure. *Proc. Natl. Acad. Sci. U. S. A.* **105**, 14779–83 (2008).

[10] French, M., Mattsson, T., Nettelmann, N. & Redmer, R. Equation of state and phase diagram of water at ultrahigh pressures as in planetary interiors. *Phys. Rev. B* **79**, 054107 (2009).

[11] Redmer, R., Mattsson, T. R., Nettelmann, N. & French, M. The phase diagram of water and the magnetic fields of Uranus and Neptune. *Icarus* **211**, 798–803 (2011).

[12] Hernandez, J.-a. & Caracas, R. Superionic-Superionic Phase Transitions in Body-Centered Cubic H_2O Ice. *Phys. Rev. Lett.* **117**, 135503 (2016).

[13] Wilson, H. F., Wong, M. L. & Militzer, B. Superionic to superionic phase change in water: consequences for the interiors of Uranus and Neptune. *Phys. Rev. Lett.* **110**, 151102 (2013).

[14] Sun, J., Clark, B. K., Torquato, S. & Car, R. The phase diagram of high-pressure superionic ice. *Nat. Commun.* **6**, 8156 (2015).

[15] French, M., Desjarlais, M. P. & Redmer, R. *Ab-initio* calculation of thermodynamic potentials and entropies for superionic water. *Phys. Rev. E* **93**, 022140 (2016).

[16] Millot, M. *et al.* Experimental evidence for superionic water ice using shock compression. *Nat. Phys.* **14**, 297–302 (2018).

[17] del Rosso, L., Celli, M. & Ulivi, L. New porous water ice metastable at atmospheric pressure obtained by emptying a hydrogen-filled ice. *Nat. Commun.* **7**, 13394 (2016).

[18] Rygg, J. R. *et al.* Powder diffraction from solids in the terapascal regime. *Rev. Sci. Instrum.* **83**, 113904 (2012).

[19] Coppari, F. *et al.* Experimental evidence for a phase transition in magnesium oxide at exoplanet pressures. *Nat. Geosci.* **6**, 926–929 (2013).

[20] Dolan, D. H. & Gupta, Y. M. Nanosecond freezing of water under multiple shock wave compression: optical transmission and imaging measurements. *J. Chem. Phys.* **121**, 9050–7 (2004).

[21] Chau, R., Mitchell, A. C., Minich, R. W. & Nellis, W. J. Electrical conductivity of water compressed dynamically to pressures of 70-180 GPa (0.7-1.8 Mbar). *J. Chem. Phys.* **114**, 1361 (2001).

[22] Dolan, D. H., Knudson, M. D., Hall, C. a. & Deeney, C. A metastable limit for compressed liquid water. *Nat. Phys.* **3**, 339–342 (2007).

[23] Gleason, A. E. *et al.* Compression Freezing Kinetics of Water to Ice VII. *Phys. Rev. Lett.* **119**, 025701 (2017).

[24] Gleason, A. E. *et al.* Ultrafast visualization of crystallization and grain growth in shock-compressed SiO2. *Nat. Commun.* **6**, 8191 (2015).

[25] Shibuta, Y. *et al.* Heterogeneity in homogeneous nucleation from billion-atom molecular dynamics simulation of solidification of pure metal. *Nat. Commun.* **8**, 1–8 (2017).

[26] Sugimura, E. *et al.* Compression of H_2O ice to 126 GPa and implications for hydrogen-bond symmetrization: synchrotron x-ray diffraction measurements and density-functional calculations. *Phys. Rev. B* **77**, 214103 (2008).

[27] French, M. & Redmer, R. Construction of a thermodynamic potential for the water ices VII and X. *Phys. Rev. B* **91**, 014308 (2015).

[28] Benoit, M., Bernasconi, M., Focher, P. & Parrinello, M. New high-pressure phase of ice. *Phys. Rev. Lett.* **76**, 2934–2936 (1996).

[29] Caracas, R. Dynamical Instabilities of Ice X. *Phys. Rev. Lett.* **101**, 1–4 (2008).

[30] Militzer, B. & Wilson, H. New Phases of Water Ice Predicted at Megabar Pressures. *Phys. Rev. Lett.* **105**, 5–8 (2010).

[31] Hermann, A., Ashcroft, N. W. & Hoffmann, R. High pressure ices. *Proc. Natl. Acad. Sci. U. S. A.* **109**, 745–50 (2012).

[32] Nettelmann, N., Helled, R., Fortney, J. & Redmer, R. New indication for a dichotomy in the interior structure of Uranus and Neptune from the application of modified shape and rotation data. *Planet. Space Sci.* **77**, 143–151 (2013).

[33] Hemley, R. J. *et al.* Static compression of H_2O-ice to 128 GPa (1.28 Mbar). *Nature* **330**, 737–740 (1987).

[34] Loubeyre, P., LeToullec, R., Wolanin, E., Hanfland, M. & Hausermann, D. Modulated phases and proton centring in ice observed by X-ray diffraction up to 170 GPa. *Nature* **397**, 503–506 (1999).

[35] Frank, M. R. M., Fei, Y. & Hu, J. Constraining the equation of state of fluid H_2O to 80 GPa using the melting curve, bulk modulus, and thermal expansivity of ice VII. *Geochim. Cosmochim. Acta* **68**, 2781–2790 (2004).

[36] Sugimura, E. *et al.* Simultaneous high-pressure and high-temperature volume measurements of ice VII and its thermal equation of state. *Phys. Rev. B* **82**, 134103 (2010).

[37] Sugimura, E. *et al.* Experimental evidence of superionic conduction in H_2O ice. *J. Chem. Phys.* **137**, 194505 (2012).

[38] Celliers, P. M. *et al.* Line-imaging velocimeter for shock diagnostics at the OMEGA laser facility. *Rev. Sci. Instrum.* **75**, 4916 (2004).

[39] Millot, M. *et al.* Shock compression of stishovite and melting of silica at planetary interior conditions. *Science* **347**, 418–420 (2015).

[40] Larsen, J. T. & Lane, S. M. HYADES − A plasma hydrodynamics code for dense plasma studies. *J. Quant. Spectrosc. Radiat. Transf.* **51**, 179–186 (1994).

[41] Swift, D. C., Tierney IV, T. E., Kopp, R. A. & Gammel, J. T. Shock pressures induced in condensed matter by laser ablation. *Phys. Rev. E - Stat. Nonlinear, Soft Matter Phys.* **69**, 1–9 (2004).

[42] Millot, M. *et al.* Measuring the shock impedance mismatch between high-density carbon and deuterium at the National Ignition Facility. *Phys. Rev. B* **97**, 144108 (2018).

[43] Orlikowski, D., Correa, A. A., Schwegler, E. & Klepeis, J. E. A Steinberg-Guinan Model for High-Pressure Carbon: Diamond Phase. *AIP Conf. Proc.* **955**, 247–250 (2008).

[44] Fratanduono, D. E., Eggert, J. H., Boehly, T. R., Barrios, M. A. & Collins, G. W. Internal target reflections and line-imaging velocimetry. *High Energy Density Phys.* **11**, 26–29 (2014).

[45] Cullity, B. D. & Stock, S. R. *Elements of X-ray Diffraction, Third Edition* (Prentice-Hall, 2001).

[46] Wang, J. *et al.* X-ray diffraction of molybdenum under ramp compression to 1 TPa. *Phys. Rev. B* **94**, 104102 (2016).

[47] Lazicki, A. *et al.* X-Ray Diffraction of Solid Tin to 1.2 TPa. *Phys. Rev. Lett.* **115**, 075502 (2015).

[48] Wicks, J. K. *et al.* Crystal structure and equation of state of Fe-Si alloys at super-Earth core conditions. *Sci. Adv.* **4**, eaao5864 (2018).

[49] Barrios, M. A. *et al.* Precision equation-of-state measurements on National Ignition Facility ablator materials from 1 to 12 Mbar using laser-driven shock waves. *J. Appl. Phys.* **111**, 093515 (2012).

[50] Hu, S. X., Boehly, T. R. & Collins, L. a. Properties of warm dense polystyrene plasmas along the principal Hugoniot. *Phys. Rev. E* **89**, 063104 (2014).

[51] Warren, B. E. & Averbach, B. L. The Effect of Cold Work Distortion on X-Ray Patterns. *J. Appl. Phys.* **21**, 595–599 (1950).

[52] Sosso, G. C. *et al.* Crystal Nucleation in Liquids: Open Questions and Future Challenges in Molecular Dynamics Simulations. *Chem. Rev.* **116**, 7078–7116 (2016). arXiv:1611.06456.

[53] Pisarev, V. V. Nonclassical nucleation kinetics in the crystallization of a supercooled melt. *Russ. J. Phys. Chem. A* **88**, 1382–1387 (2014).

[54] Shen, Y., Jester, S. B., Qi, T. & Reed, E. J. Nanosecond homogeneous nucleation and crystal growth in shock-compressed SiO2. *Nat. Mater.* (2015).

[55] Zhao, S. *et al.* Amorphization and nanocrystallization of silicon under shock compression. *Acta Mater.* **103**, 519–533 (2016).

[56] Huang, F., Zhang, H. & Banfieldt, J. F. Two-stage crystal-growth kinetics observed during hydrothermal coarsening of nanocrystalline ZnS. *Nano Lett.* **3**, 373–378 (2003).

[57] Dewaele, A., Loubeyre, P. & Mezouar, M. Equations of state of six metals above 94 GPa. *Phys. Rev. B* **70**, 094112 (2004).

[58] Goldman, N., Fried, L., Kuo, I.-F. & Mundy, C. Bonding in the Superionic Phase of Water. *Phys. Rev. Lett.* **94**, 217801 (2005).

[59] French, M., Mattsson, T. & Redmer, R. Diffusion and electrical conductivity in water at ultrahigh pressures. *Phys. Rev. B* **82**, 1–9 (2010).

[60] French, M., Hamel, S. & Redmer, R. Dynamical Screening and Ionic Conductivity in Water from Ab Initio Simulations. *Phys. Rev. Lett.* **107**, 185901 (2011).

[61] Hermann, A., Ashcroft, N. W. & Hoffmann, R. Isotopic differentiation and sublattice melting in dense dynamic ice. *Phys. Rev. B* **88**, 214113 (2013).

[62] Hernandez, J.-A. & Caracas, R. Proton dynamics and the phase diagram of dense water ice. *J. Chem. Phys.* **148**, 214501 (2018).

[63] Pickard, C. J., Martinez-Canales, M. & Needs, R. J. Decomposition and Terapascal Phases of Water Ice. *Phys. Rev. Lett.* **110**, 245701 (2013).

[64] McMahon, J. Ground-state structures of ice at high pressures from ab initio random structure searching. *Phys. Rev. B* **84**, 1–4 (2011).

[65] Ji, M. *et al.* Ultrahigh-pressure phases of H_2O ice predicted using an adaptive genetic algorithm. *Phys. Rev. B* **84**, 220105(R) (2011).

[66] Hermann, A. & Schwerdtfeger, P. Blueshifting the onset of optical UV absorption for water under pressure. *Phys. Rev. Lett.* **106**, 1–4 (2011).

[67] Zhang, S., Wilson, H. F., Driver, K. P. & Militzer, B. H_4O and other hydrogen-oxygen compounds at giant-planet core pressures. *Phys. Rev. B - Condens. Matter Mater. Phys.* **87**, 1–5 (2013). arXiv:1209.3448.

[68] Salzmann, C., Radaelli, P. G., Hallbrucker, A., Mayer, E. & Finney, J. L. New hydrogen ordered phases of ice. *Science* **311**, 1758–1761 (2007).

[69] Salzmann, C. G., Radaelli, P. G., Mayer, E. & Finney, J. L. Ice XV: A new thermodynamically stable phase of ice. *Phys. Rev. Lett.* **103**, 1–4 (2009).

[70] Komatsu, K. *et al.* Partially ordered state of ice XV. *Sci. Rep.* **6**, 28920 (2016).

[71] Falenty, A., Hansen, T. C. & Kuhs, W. F. Formation and properties of ice XVI obtained by emptying a type sII clathrate hydrate. *Nature* **516**, 231–233 (2014).

[72] Sha, X. & Cohen, R. E. Thermal effects on lattice strain in ϵ-Fe under pressure. *Phys. Rev. B - Condens. Matter Mater. Phys.* **74**, 1–26 (2006).

[73] Kresse, G. & Hafner, J. Ab initio molecular dynamics for liquid metals. *Phys. Rev. B* **47**, 558–561 (1993).

[74] Blöchl, P. E. Projector augmented-wave method. *Phys. Rev. B* **50**, 17953–17979 (1994). arXiv:arXiv:1408.4701v2.

[75] Kresse, G. & Joubert, D. From ultrasoft pseudopotentials to the projector augmented-wave method. *Phys. Rev. B* **59**, 1758–1775 (1999).

[76] Nosé, S. A unified formulation of the constant temperature molecular dynamics methods. *J. Chem. Phys.* **81**, 511–519 (1984).

[77] Hoover, W. G. Canonical dynamics: Equilibrium phase-space distributions. *Phys. Rev. A* **31**, 1695–1697 (1985).

[78] Perdew, J. P., Burke, K. & Ernzerhof, M. Generalized gradient approximation made simple. *Phys. Rev. Lett.* **77**, 3865–3868 (1996).

[79] Hill, R. The elastic behaviour of a crystalline aggregate. *Proc. Phys. Soc. Sect. A* **65**, 349–354 (1952).